Published in final edited form as:

Phys Rev E. 2023 July ; 108(1-1): 014408. doi:10.1103/PhysRevE.108.014408.

Metal-pad-enhanced resistive pulse sensor reveals complex-valued Braess paradox

Alan Dong,

Department of Electrical Engineering and Computer Sciences, University of California, Berkeley, Berkeley, California 94720, USA

Lydia Sohn,

Department of Mechanical Engineering, University of California, Berkeley, Berkeley, California 94720, USA

Michael Lustig

Department of Electrical Engineering and Computer Sciences, University of California, Berkeley, Berkeley, California 94720, USA

Abstract

A resistive pulse sensor measures the electrical impedance of an electrolyte-filled channel as particles flow through it. Ordinarily, the presence of a nonconductive particle increases the impedance of the channel. Here we report a surprising experimental result in which a microfluidic resistive pulse sensor experiences the opposite effect: The presence of a nonconductive particle decreases the channel impedance. We explain the counterintuitive phenomenon by relating to the Braess paradox from traffic network theory, and we call it the complex-valued Braess paradox (CVBP). We develop theoretical models to study the CVBP and corroborate the experimental data using finite element simulations and lumped-element circuit modeling. We then discuss implications and potential applications of the CVBP in resistive pulse sensing and beyond.

I. INTRODUCTION

Resistive pulse sensing (RPS) [1–4] has long been a favored technology for microfluidic cytometry due to its simple sensing mechanism based on measuring electrical impedance. When a nonconductive particle, e.g., a cell, flows through a narrow channel, or “pore,” the impedance magnitude measured across the channel temporarily increases, creating the eponymous resistive pulse. Node-pore sensing (NPS) [5] introduced the concept of deliberately widening certain regions within the channel such that when the cell flows through a wide region, or “node,” the measured impedance decreases back toward the baseline (i.e., the measured impedance with no cell present). In order to replicate the impedance modulation behavior of NPS without using channel width modulation, we developed a technology called “metal pad sensing” (MPS). Instead of introducing wider regions within the channel, we pattern floating-potential metal pads within a channel of constant width. When the cell flows over the metal pad, we expect electric current to bypass the cell using the metal pad as a low-impedance parallel path, resulting in an impedance decrease back toward the baseline, similar to the case of a node in NPS. However, we observed a puzzling result: Under certain conditions, the impedance decreases to below the

baseline! In other words, the presence of a cell decreased the channel impedance magnitude, contrary to a typical RPS device. This is surprising because physical intuition suggests that a nonconductive particle can only increase the channel impedance by blocking current paths. In this paper, we explain this paradoxical phenomenon, which we call the "complex-valued Braess paradox" (CVBP). We first develop its theory using electrical circuit models, and then corroborate the empirical data using both lumped-component circuit models and finite element analysis. We conduct a detailed study of the variables affecting the paradox using validation devices. Finally, we discuss the implications and potential applications of the CVBP.

A. Resistive pulse sensing

We observe the CVBP in a microfluidic platform, which we call the metal pad sensing device. MPS is based on RPS, a ubiquitous and powerful technology for counting and sizing particles suspended in electrolyte solution. RPS consists of two reservoirs connected by an aperture or narrow channel. Particles in solution flow through the channel while the electrical impedance between the reservoirs is continuously measured. When a nonconductive particle enters the channel, it causes the resistance to increase temporarily, creating a "resistive pulse." The magnitude of the pulse is proportional to the volume ratio of the particle and channel ($\Delta R/R \propto V_{\text{particle}}/V_{\text{channel}}$). Analysis of the impedance vs time through signal processing results in the number of particles in a measured volume and a distribution of sizes. When particles of interest are cells, this technique is called resistive pulse cytometry [6]. RPS has been used to determine cell size [7,8], identify cell surface markers [5,9], characterize cell biophysical properties [10–13], and measure cell membrane capacitance and cytoplasm conductivity [14–16]. These properties can provide important insight into fundamental biology and potentially inform clinical diagnoses.

B. Metal pad sensing

Figures 1(a) and 1(b) show the MPS device, which consists of two reservoirs joined by a narrow channel. The channel is embedded in a polydimethylsiloxane (PDMS) slab via soft lithography and bonded to a glass substrate with prefabricated metal electrodes (50 Å Ti/500 Å Pt). One pair of electrodes, outside of the channel but transverse to the reservoirs, allows us to apply a voltage across the channel. A floating-potential "metal pad," positioned at the center of the channel, does not source or sink net current and therefore is not considered an electrode. This metal pad, however, does provide a current path in parallel with the bulk electrolyte solution that fills the channel. We refer to the segment of the channel containing the metal pad as the "pad segment" and the two segments of the channel outside of the pad segment as "gaps" [Fig. 1(c)]. Inlet and outlet holes are punches through the reservoirs at both ends of the device, thereby providing inlet and outlet access and completing the device. MCF-7 cells (ATTC), 18.9μm mean diameter and suspended in phosphate-buffered saline (PBS) at a concentration of 4.44×10^5 cells /mL, flowed through the channel at a constant pressure of 5mbar at the inlet using an OB1 flow controller (Elveflow, Paris, France).

A 3.82-V peak-to-peak multisine stimulus potential consisting of four frequencies (1,10,50, and 400 kHz with phases of −90◦,0◦,90◦, and 180◦, respectively) was applied across the electrodes [Fig. 1(c)]. The resulting current was measured using a transimpedance amplifier

and sampled with a PCI-6251 data acquisition system (DAQ) (National Instruments, Austin, TX) at a rate of 1MHz, digitally quadrature demodulated at each frequency, and digitally filtered to remove noise and interference. The impedance Z at each frequency was calculated as $Z = -R_{\mathrm{TIA}}\left(\widetilde{V}_{\mathrm{stim}}/\widetilde{V}_{\mathrm{filt}}\right)$, where R_{TIA} is value of the transimpedance gain resistor, $\widetilde{V}_{\mathrm{stim}}$ is the stimulus voltage phasor, and $\widetilde{V}_{\mathrm{filt}}$ is the voltage phasor measured at the DAQ, after filtering.

Figure 1(d) shows impedance magnitude vs time for an MCF-7 cell transiting the channel, with each portion of the impedance signal highlighted according to whether the cell is traversing a gap [red (darker)] or pad segment [yellow (lighter)]. Due to imperfections during the device fabrication process, the first gap's portion of the signal is larger in amplitude and shorter in duration than that of the second. At all frequencies, the cell's presence in the gaps causes the impedance to increase, consistent with the principles of RPS. When the cell traverses the pad segment, the impedance decreases toward baseline, with greater decrease at higher frequencies. At 50 kHz, we observe the paradoxical phenomenon: The impedance actually dips *below* the baseline by −0.71%. In other words, the presence of a cell, which is considered a nonconducting particle at frequencies below 1MHz [17], *decreases* the channel impedance, but only when a metal pad is also present. We call this phenomenon the complex-valued Braess paradox, which we explain in greater detail in the following sections. The concept of RPS impedance modulation using floating-potential metal pads was first proposed by De Ninno *et al.* [18]; however, no CVBP was observed, likely because the metal pads were too short (30μm), the frequency was too high (⩾0.5MHz), and the particles were too small (⩽8μm diameter within a 40μm × 21μm cross-section channel). The CVBP's dependence on metal pad length, frequency, and particle size will be explained in Sec. II A and validated in Sec. III.

C. Reproducibility

We have provided raw data, analysis code, and plotting scripts (all in MATLAB) for generating figures at [19]. The same repository also contains our MPS device COMSOL model and AutoCAD drawings of the photolithography masks used to fabricate our devices. Software is additionally provided in a GitHub repository [20].

D. Braess paradox

We explain the counterintuitive phenomenon observed in our MPS experiments through the Braess paradox from transportation network theory. The classical Braess paradox [21] states that the addition of a path to a congested traffic network can counterintuitively increase congestion instead of allowing a more efficient flow distribution. An example network is shown in Fig. 2(a). Users travel from the left node to the right node, and each path has a different cost. Specifically, traversing path i has a cost C_i (travel time in minutes) that is a function of its flow f_i (number of users per unit time). Paths a and d (taxi) have cost functions $C_a = 10f_a$ and $C_d = 10f_d$. Paths b and c (walking) have cost functions $C_b = f_b + 40$ and $C_c = f_c + 40$. Path e (high-speed train) has negligible cost $C_e = 0$.

Suppose that, in one unit of time, four users travel through the network. If path e is absent (represented as an open switch), solving the equilibrium flow is straightforward: Two users take path ab, two users take path cd, and both paths cost $C_{ab} = C_{cd} = 10(2) + (2) + 40 = 62$

minutes. If we close the switch to add path e, the equilibrium shifts. Each user has a selfish incentive to switch to path *aed* to improve their own cost at the expense of all others. Ultimately, every user takes path *aed*, which costs $C_{aed} = 10(4) + 0 + 10(4) = 80$ minutes, and has no incentive to switch back. The system reaches a stable but suboptimal equilibrium. This is the essence of the Braess paradox.

Braess and Braess-like paradoxes have been described and studied in a wide range of fields: Communication networks [22,23], distributed computer systems [24], power grids [25,26], mesoscopic physics [27,28], quantum physics [29,30], fluid dynamics [31], biological systems [32,33], and electrical and mechanical systems [34]. Most relevant are electrical analogs of the Braess paradox. For example, in the DC circuit shown in Fig. 2(b), current and voltage replace "flow rate" and "cost," respectively, and electrical charges are the network users. The equations governing the circuit (Ohm's law and Kirchhoff's voltage and current laws) take the same form as in the traffic example. With $I = 4$ A, $R_a = 10\Omega$, $R_b = 1\Omega$, and $V_b = 40$ V, the equations become identical and the same paradox occurs: Closing switch e counterintuitively increases the voltage V from 62 to 80 V.

An analysis of the Braess paradox in several DC circuits is presented in [35] along with experimental confirmation using only passive components (Zener and Shockley diodes) to implement near-constant voltage drops.

In the following sections, we will analyze several circuit models that more closely resemble our single-pad MPS device. We use these models as stepping stones on our journey to connect the classical Braess paradox to the CVBP that we originally observed in our experiments.

E. Complex-valued Braess paradox

We present a new Braess-like paradox that occurs in two-port AC circuit networks. The "flow rate" is the current magnitude and the "cost" is the voltage magnitude, since both current and voltage are complex phasors. If the circuit contains only passive, linear elements, then the voltage across the circuit's two ports is directly proportional to the current through them, and the ratio of voltage to current is the circuit's equivalent complex impedance. The CVBP is thus: The addition of a path to a circuit containing only passive, linear components (and no resonance) can counterintuitively increase the magnitude of the circuit's total impedance. While the paradox could alternatively be defined using the real part (resistance) or imaginary part (reactance) of the impedance, we will focus, instead, on the magnitude for simplicity and consistency.

Figure 2(c) shows a symmetric RC bridge circuit example. With switch e open, the circuit is a parallel combination of two identical series RC circuits. With switch e closed, the circuit becomes a series combination of two identical parallel RC circuits. Solving for both impedances at the RC cutoff frequency $\omega = 1/RC$, we obtain

$$Z_{\text{open}}\left(\omega = \frac{1}{RC}\right) = \frac{1}{2}\left(R + \frac{1}{j\omega C}\right) = \frac{R\sqrt{2}}{2}\angle -45^\circ,$$

$$Z_{\text{closed}}\left(\omega = \frac{1}{RC}\right) = 2\left(\frac{1}{1/R + j\omega C}\right) = R\sqrt{2}\angle -45^\circ.$$

At the cutoff frequency, adding path e increases the impedance magnitude by a factor of 2 while the phase angle stays the same. The cutoff frequency satisfies the CVBP, but not all frequencies do. The open-switch and closed-switch impedance spectra are plotted in Fig. 2(c) as normalized impedance magnitude $|Z|/R$ vs normalized frequency ωRC, both unitless quantities on a logarithmic scale. We call the region around $\omega RC = 1$ in which the paradox occurs the "paradoxical region" and find its boundary points by solving the quadratic $|Z_{\text{open}}(\omega)| = |Z_{\text{closed}}(\omega)|$ in ω. The CVBP occurs when $2 - \sqrt{3} \approx 0.268 < \omega RC < 3.732 \approx 2 + \sqrt{3}$, and achieves a maximum paradoxical increase of a factor of 2 at $\omega RC = 1$. The analytical impedances are corroborated with experimental data (plotted as circles).

Figure 2(d) shows another example, which we call the "R + C/(R)" circuit. It is identical to the previous circuit but missing one capacitor. We again calculate Z_{open} and Z_{closed}, whose expressions are omitted for brevity. In short, the CVBP occurs when $\omega RC > 1/\sqrt{2} \approx 0.707$, and achieves a maximum paradoxical increase of a factor of $\sqrt{4/3} \approx 1.155$ at $\omega RC = \sqrt{2} \approx 1.414$. The removal of the second capacitor decreases the strength of the CVBP and shifts the paradoxical region. Again, the analytical impedances are corroborated with experimental data.

The R + C/(R) circuit constitutes the simplest lumped-component circuit model of the single-pad MPS device. The closed-switch circuit is a resistor in series with a parallel RC circuit, denoted as "R + C/R." When the switch is opened, the circuit changes to "R + C." Similarly, in the single-pad MPS device, a cell entering the pad segment causes a change between two states, which we call "no cell" and "cell over pad." In the "no cell" state, the pad segment, shown superimposed on the circuit in Fig. 2(d), can be approximated as a parallel R/C circuit. The path through the electrolyte solution is purely resistive (at low frequencies) while the path through the metal pad bypassing the electrolyte solution is mostly capacitive due to the electrical double layer (EDL) [36]. The voltage electrodes also have an EDL capacitance; however, their impedance contribution is negligible at our frequencies of interest, and we can exclude them from the model. Finally, the electrolyte solution in the gaps presents a series resistance. Thus, the "no cell" state corresponds to the R + C/R circuit, and the "cell over pad" state corresponds to the R + C circuit. This assumes that the cell completely blocks the resistive path, acting like an open switch. This is the inverse of the CVBP as previously described: Removing one path from the circuit paradoxically *decreases* the impedance magnitude.

F. Differential complex-valued Braess paradox

While the R + C/(R) circuit model is useful for connecting the Braess paradox to the real single-pad MPS device, a cell in the pad segment acts nothing like an open switch. In fact, it only increases the local resistance by a small amount which can be predicted from cell diameter and channel geometry using formulas from classical RPS theory [2,3,37,38]. In practice, the resistance increase is typically only a few percent of the total channel

impedance magnitude. Therefore, we require a different circuit model to study how small resistance changes affect total impedance magnitude.

Figure 2(e) shows an R + R(+ ΔR)/C circuit that has a variable resistor R_e. Unlike in the previous circuit [Fig. 2(d)], the resistance in parallel does not switch from R to infinity. Instead, R_e increases by ΔR_e. Consequently, the total impedance magnitude $|Z|$ changes by $\Delta|Z|$. When the change in R_e is infinitesimally small, the impedance magnitude changes according to the derivative $\partial|Z|/\partial R_e$. Because the CVBP occurs in the R + C/(R) circuit and $|Z|$ is a continuous differentiable function of R_e, then there must exist values of R_e between R and ∞ at which $\partial|Z|/\partial R_e$ is negative-increasing R_e *decreases* $|Z|$. We call this phenomenon the differential complex-valued Braess paradox (DCVBP). Figure 2(e) plots the derivative $\partial|Z|/\partial R_e$ against frequency (normalized by the time constant R_eC and logarithmically scaled) for different values of R_e (normalized by R). As R_e becomes small relative to R, the DCVBP becomes stronger and the paradoxical region grows. As R_e becomes large, the paradox asymptotically disappears. When $R_e = R$, the DCVBP occurs at frequencies $\omega R_eC > \sqrt{2} \approx 1.414$ and achieves a maximum paradoxical effect of approximately −68.53 mΩ/Ω at $\omega R_eC \approx 2.358$.

This analysis also allows us to address small, finite changes in R_e, such as those caused by a cell transit event in our single-pad MPS device. Any finite change in $|Z|$ caused by a finite change in R_e can be calculated by the integration

$$\Delta|Z| = \int_{R_e}^{R_e + \Delta R_e} \frac{\partial|Z|}{\partial r} dr .$$

Alternatively, we can calculate $\Delta|Z|$ directly from the circuit with

$$\Delta|Z| = \left| \frac{1}{\frac{1}{(R_e + \Delta R_e)} + j\omega C} \right| - \left| \frac{1}{\frac{1}{R_e} + j\omega C} \right| .$$

When any positive ΔR_e results in a negative $\Delta|Z|$, we will also refer to that as a CVBP. Thus, the definition of the CVBP can be expanded as follows: Increasing the impedance of a path in a circuit containing only passive, linear components (and no resonance) can counterintuitively decrease the magnitude of the circuit's total impedance.

Figure 2(f) displays both the CVBP and DCVBP on the same plot. For the circuit in Fig. 2(e), we plot $\Delta|Z|$ vs ΔR_e for the case where $R_e = R$. The values on both axes are expressed as a percentage of the baseline impedance magnitude $|Z|$. Each curve shows a different frequency, normalized by the time constant R_eC. Any point in the bottom right quadrant of the plot indicates CVBP, while any point at which the tangent line has negative slope indicates DCVBP. This type of diagram will prove insightful for studying our MPS devices.

II. METHODS

While we established a theoretical framework to explain the CVBP in our original MPS experiments, we seek a deeper understanding of the phenomenon and the factors that affect it. Therefore, we require (1) a higher-fidelity MPS device model to make predictions based on our theory and (2) experimental validation.

A. Higher-fidelity MPS models

The circuit model of the form R + R/C is straightforward to analyze and demonstrates the CVBP, but it is too simplistic to accurately predict the behavior of real MPS devices. For a more accurate, higher-fidelity model, we performed finite element analysis (FEA) of a simulated single-pad MPS device. Specifically, we defined the device as a rectangular prism of width $W = 10$ μm and height $H = 20$ μm, filled with PBS. A metal pad of length $L_P = 80$ μm at the center of the channel divided the channel into two gaps of length $L_G = 40$ μm. A side view for three different cell positions within the channel is shown (not to scale) in the third column of Fig. 3(a). We then defined a constant-magnitude AC current of $\tilde{I} = 1$ μA through the channel, and calculated the voltage $\tilde{V}$ between the leftmost plane of the first gap and the rightmost plane of the second gap. We computed impedance as the ratio of voltage to current, $Z = \tilde{V}/\tilde{I}$. We modeled the EDL between the metal pad and PBS as a distributed impedance with zero conductivity $\sigma = 0$ S/m and specific capacitance (i.e., capacitance per unit area) $C_s = 0.2$ F/m^2. We defined the PBS with resistivity $\rho = 0.625$ Ωm and relative permittivity $\epsilon_r = 70$ and modeled the cell as a sphere with zero conductivity $\sigma = 0$ S/m and $\epsilon_r = 60$. In the case that the cell's spherical diameter exceeds the channel width, we assume that it deforms into an oblate spheroid of equal volume. We consider any impedance contributions originating from outside of the channel, including the EDL between the PBS and the electrodes V_+ and V_-, to be negligible.

A fully 3D FEA model is computationally expensive, so we also sought to develop a lumped-component circuit (LCC) model that can closely match the FEA model. The first of two models we developed is called the LCC slice model [second column of Fig. 3(a)], which can be understood as a straightforward extension of the R + R/C model [first column of Fig. 3(a)]. To better approximate the distributed nature of the metal pad's EDL impedance, we make $N + 1$ "slices" (represented by dashed lines) to divide the pad segment into N identical "blocks" along its length, such that each block is a rectangular prism of length $l_P = L_P/N$, width W, and height H, and each slice is a $W \times H$ rectangle. Each slice is assumed to be an isopotential surface, represented by a circuit node called a "slice node." Each metal pad is also an isopotential surface, represented by a circuit node called a "pad node." For each pad segment, every slice node is connected to the underlying pad node via a capacitance $c_P = C_s l_p W$. The edge cases of the leftmost and rightmost slices have half the capacitance. Next, adjacent slice nodes are connected via a resistance $r_P = \rho l_P/(WH)$. The resistance across each gap is similarly modeled as $R_G = \rho L_G/(WH)$. When a cell is present in the channel, it introduces a purely resistive increase ΔR. Because equations from classical RPS theory [37] do not consider particle sizes exceeding the channel size, we compute ΔR with FEA simulation. Finally, this ΔR is distributed between the block resistances r_P and/or

gap resistances R_G according to the proportion of the cell's volume occupying each block and/or gap. For example, in the third row of Fig. 3(a), the cell is shown occupying two blocks: Block n and block $n+1$, with proportion p_n of its volume in block n and proportion $p_{n+1} = 1 - p_n$ of its volume in block $n+1$. The resistance of block n increases by $p_n \Delta R$ and the resistance of block $n+1$ increases by $(1 - p_n)\Delta R$.

The second and more accurate LCC model we developed is called the LCC voxel model. The main difference between the slice model and the voxel model is that the latter allows for curved isopotential surfaces, which occur wherever electric field lines curve to enter a metal pad [as shown in the third column of Fig. 3(a)]. The full details of the voxel model are presented in the Appendix, but the basic concept is that each gap or pad segment is divided along its length *and* its height to form a two-dimensional (2D) array of voxels. The voxel edges oriented perpendicular to the page (line segments of length) are assumed to be isopotentials, and are represented by circuit nodes called "voxel nodes." Adjacent voxel nodes are connected via resistors, and voxels located above a metal pad have their voxel nodes connected to the corresponding pad node via capacitors. The presence of a cell is modeled by increasing the resistance of each resistor in proportion to the partial volume of the cell contained within the volume of that resistor's corresponding voxels, such that the total channel resistance increases by ΔR, which is computed from FEA simulation. Finding the correct resistance values to achieve the desired ΔR is nontrivial and requires multiple iterations of solving for hundreds or thousands of node voltages and branch currents. Although the LCC voxel model is more computationally expensive than the LCC slice model, it closely matches the FEA model with much less computation.

Figure 3(a) shows the LCC slice model and FEA model under three distinct conditions: "no cell," "cell in gap," and "cell over pad." The R + R/C model is also shown for reference. Figure 3(b) compares different models' predicted impedance spectra as Bode and Nyquist plots reflecting the three conditions, with a $d = 13.39$ μm diameter cell causing a ΔR of 9.86% over the baseline for all four models. For this comparison, the R + R/C model used $C = C_s L_p W/10$, the LCC slice model used $N = 250$, and the LCC voxel model used voxels of size $1.818\ \mu\text{m} \times 10\ \mu\text{m} \times 1.818\ \mu\text{m}$ ($L \times W \times H$). The CVBP is predicted in all four models, but not at the same frequency. The R + R/C model predicts 52.7 kHz as the start of the paradoxical region, the LCC slice model predicts 29.8 kHz, and the LCC voxel model and FEA model both predict 34.5 kHz.

Figure 3(c) directly compares the LCC voxel model and FEA model using a "pad vs gap response diagram," which is similar to the diagram in Fig. 2(f), but with one minor deviation. The horizontal axis now plots the normalized change in impedance magnitude when the cell occupies a gap, which is almost equal to ΔR. The vertical axis is the same as in Figure 2(f), but more explicitly spelled out to be the normalized change in impedance magnitude when the cell is directly over the metal pad. We define $(|Z_{\text{gap}}| - |Z_{\text{none}}|)/|Z_{\text{none}}|$ as the "gap response" and $(|Z_{\text{pad}}| - |Z_{\text{none}}|)/|Z_{\text{none}}|$ as the "pad response." For each frequency, plotting pad response against gap response produces a pad vs gap response curve. A collection of such curves forms the pad vs response diagram [Fig. 3(c)], which shows that the LCC voxel model and FEA model agree very well, especially for smaller cell diameters. Compared

to the R + R/C model, whose pad vs gap response diagram would look nearly identical to Fig. 2(f), the LCC voxel model and FEA model predict stronger paradoxical effects, with a maximum DCVBP slope of approximately −83 mΩ/Ω at 61.7 kHz.

One major difference between the LCC voxel model and the FEA model is that the former, computed using LTSPICE, is capable of replacing each capacitor with a constant phase element (CPE). A CPE can be regarded as a nonideal capacitor, with an impedance defined by $Z_{\mathrm{CPE}} = 1/\left((j\omega)^{\alpha}Q\right)$, where Q is the CPE parameter, analogous to capacitance, and α is the CPE exponent, which can be understood as an ideality constant. When $\alpha = 1$, the CPE becomes an ideal capacitor and Q is its capacitance. When $\alpha = 0$, the CPE becomes a resistor and Q is its conductance. In practice, a polarizable electrode/electrolyte interface, such as Pt/PBS, can be accurately modeled by a CPE with $\alpha < 1$ [39]. The FEA model implemented using COMSOL does not have this capability. Since the LCC voxel model performs similarly to the FEA model, is much faster to compute, and has the added flexibility of using CPEs, it is our model of choice for simulating MPS devices.

From our LCC models of MPS devices, we can gain intuition about the factors affecting the extent to which the CVBP (and DCVBP) occur when a cell traverses over a metal pad. The two primary factors are (1) cell size relative to channel size and (2) stimulus frequency relative to a critical frequency of the pad segment. We expect that, for a given MPS channel, the larger the cell is, the larger the ΔR is, and the stronger the CVBP can be. We also expect the existence of a paradoxical region for the DCVBP starting at some critical frequency. At frequencies below the critical frequency, introducing a cell will increase the impedance magnitude. At or above the critical frequency, the DCVBP occurs; introducing a cell will decrease the impedance magnitude. As frequency increases, the DCVBP should asymptotically disappear.

The actual value of the critical frequency should vary inversely with an RC time constant of the pad segment based on its geometry and electrical properties. For example, if the resistivity of the electrolyte solution increases, the RC time constant increases, and the critical frequency should decrease, assuming the specific capacitance (or specific CPE parameter and CPE exponent) of the metal pad EDL is unaffected. Alternatively, if the specific capacitance increases, the critical frequency should also decrease. If the length of the metal pad increases, both R and C of the pad segment increase, and the critical frequency should therefore decrease. This means that very long metal pads may show the CVBP even at low frequencies while very short metal pads may require much higher frequencies to observe any impedance modulation.

B. Metal pad array devices

To investigate the effects of metal pad length, stimulus frequency, and cell size on impedance modulation in real MPS devices, we designed the metal pad array device, which has multiple metal pads of varying length patterned within a long channel. As a straightforward concatenation of single-pad MPS channels, the metal pad array device has a total channel impedance that is simply the series combination (i.e., sum) of the impedance contributions of each individual single-pad MPS channel. When a cell enters a pad segment,

it only increases the *local* impedance, so the impedance contributions of all other pads and gaps can be considered constant. Therefore, if the cell causes the total measured impedance to decrease, then the CVBP occurs for that particular triplet of metal pad length, stimulus frequency, and cell size.

We fabricated two different sizes of a "metal pad array" device: A narrower device with a channel 20.0 μm × 21.5 μm ($W \times H$), and a wider device with a channel 24.2 μm × 28.5 μm ($W \times H$). Device fabrication was as described in Sec. I B. Both devices have a total channel length of $L_{\text{total}} = 1590$ μm, comprising seven pad segments of lengths 10, 20, 40, 80, 160, 320, and 640μm separated by gaps $L_G = 40$ μm long. A pair of 1000μm × 1000μm electrodes is located outside of the channel. Metal traces connect the electrodes to contact pins that interface with the impedance measurement system. A microscope image of the wider pad array device is shown in Fig. 4(a).

MCF-7 cells (ATTC), 18.9μm mean diameter suspended in PBS at a concentration of 4.44×10^5 cells /mL, flowed through the device at a constant pressure of 1mbar at the inlet using a microfluidic flow controller. To remove temporary obstructions caused by cellular debris, large cells, or clusters of cells, the pressure was occasionally increased. While the cells were flowing through the device, the impedance at several specific frequencies was continuously measured.

C. Multisine impedance measurement

A two-point impedance measurement was performed using the circuit shown in Fig. 1(c) with a transimpedance gain resistor of $R_{\text{TIA}} = 1.00$ MΩ. The stimulus voltage V_{stim} was a multisine waveform consisting of seven cosines with frequencies 2.5, 6.5, 14.5, 34.5, 85.5, 204.5, and 498. 5 kHz and phases 0◦, 128.767◦, 152.721◦, 39.408◦, 316.434◦, 290. 386◦, and 160.713◦, respectively. The frequencies were selected to be approximately logarithmically spaced and to avoid potential interference from intermodulation products and nearby electrical equipment. The phases were numerically optimized via gradient descent with repeated random initialization to minimize the peak-to-peak amplitude of the multisine waveform. Each constituent cosine had a peak-topeak voltage of 400 mV, adding up to a multisine peak-to-peak voltage of 2.11 V. The resulting current flowing through the channel was converted to a voltage using the transimpedance amplifier and sampled at a rate of 1 MHz by the DAQ, which also generated the stimulus voltage waveform at the same sampling rate. The sampled voltage waveform V_{meas} was digitally quadrature demodulated multiple times to extract the voltage phasor $\widetilde{V}_{\text{meas}}$ at each frequency. The measured voltage phasors were then digitally filtered to remove noise and interference, resulting in $\widetilde{V}_{\text{filt}}$. The impedance Z at each frequency was calculated as $Z = -R_{\text{TIA}}\left(\widetilde{V}_{\text{stim}}/\widetilde{V}_{\text{filt}}\right)$. Finally, the impedance measurements were compensated using open and reference load compensation [40] to reduce artifacts caused by stray capacitances in the measurement circuit.

III. RESULTS

Impedance signals from two example cell transit events are shown in Fig. 4(b) as normalized impedance magnitude with respect to the baseline vs time. Only six frequencies are shown

because the highest frequency was outside of the bandwidth of the circuit and suffered from excessive noise and impedance artifacts. From left to right, we can see the cell traversing the channel, passing through each gap and pad segment, highlighted in red (dark gray) and yellow (light gray), respectively. The shape of the signal is as expected. At the lowest frequency, there is very little impedance modulation except for the longest metal pads. As the frequency increases, the degree of modulation begins to increase for all pad lengths. At 14.5 kHz, we observe the first sign of CVBP with the cell over the 640-μm-long metal segment. Focusing only on the 640-μm-long pad response, we observe that as the frequency continues to increase, the CVBP initially becomes more apparent, then asymptotically disappears. The same trend is observed for the shorter-length metal pads, but with each experiencing the CVBP within a different frequency range.

A. Data processing

To analyze the modulation behavior of each cell transit event, we employed a variety of signal processing and optimization techniques. First, the compensated impedance signal was low-pass filtered to 250 Hz bandwidth. A template of a typical cell transit event was constructed and used in a correlation-based detector to detect transit events automatically in the data. The template was stretched or compressed to many different temporal durations and the detection process was repeated to account for transit events with different transit times. Automatically detected events were ranked by normalized correlation coefficient [41], manually vetted to remove false positives and coincident events, and saved for further processing. Although we now had the start time and end time of each event, we could not automatically measure the gap response and pad response values due to shape mismatch between the signal and the template caused by nonuniform velocity during transit. A cell may experience slight acceleration or deceleration as it traverses the channel, causing temporal distortion in its transit signal. Meanwhile, a larger or stiffer cell may take a non-negligible amount of time to deform before it can squeeze into the channel, causing the first gap's portion of the signal to be temporally elongated. Both of these factors were taken into account by utilizing a deformable transit signal model, which included an acceleration term as well as a deformation time term as parameters. We used nonlinear least squares optimization to find the temporal parameters that minimized the mean absolute error (MAE) between the deformable template and each transit signal, thus refining our estimates for the start times and end times of each gap portion and metal pad portion of the transit signal.

We extracted all gap and pad response values from each transit signal by computing the average impedance magnitude within a window located at the center of each gap or metal pad portion of each signal, leading to eight gap measurements and seven metal pad measurements per transit. We estimated the "no cell" baseline impedance by averaging the values immediately before and immediately after the transit event. Finally, for each metal pad portion of the signal, we averaged the two "cell in gap" magnitudes immediately to the left and right, subtracted the baseline magnitude, then divided by the baseline magnitude to arrive at the gap response as previously defined. The pad response was similarly computed by taking the "cell over pad" magnitude, subtracting the baseline magnitude, then dividing by the baseline magnitude. This pad and gap response measurement process was repeated

for every frequency channel, resulting in 42 gap response values and 42 pad response values for each cell transit event (6 frequencies × 7 metal pad lengths).

B. Pad versus gap response diagram

We analyze the impedance modulation at each frequency for each metal pad length using pad vs gap response diagrams as described in Sec. II A. Figure 4(c), left, illustrates the construction of the response diagram for the 320-μm long pad. Gap response and pad response values (g_i and p_i) are extracted from the impedance signal at a frequency of 34.5 kHz [Fig. 4(b), left column, fourth row]. The response value corresponding to the 320-μm-long pad is denoted as p_6 [purple (dark gray) diamond]. The average of its two neighboring gap response values is $(g_6 + g_7)/2$ [purple (dark gray) squares]. Thus, on the response diagram, a point is placed at $(g_6 + g_7)/2, p_6)$ to represent 34.5 kHz [purple (dark gray)]. The same process is repeated to place a point representing 85.5 kHz [green (light gray)]. We now consider a different, larger cell [Fig. 4(b), right column], with gap and pad response values denoted using uppercase G_i and P_i. The same process produces two more points, one purple (dark gray) and one green (light gray). After this entire procedure is repeated for many cells of different sizes, the points trace out pad vs gap response curves at each frequency, which begin to resemble the analytical and simulated curves in Fig. 3(c). The pad vs gap response diagrams for all other metal pad lengths, including the 640-μm-long pad [Fig. 4(c), right], are constructed in the same manner.

Figure 5(a) shows response diagrams for the narrower metal pad array device and Fig. 5(b) shows response diagrams for the wider metal pad array device. For both devices, plots of the 10-μm-long metal pads are not shown because they are not significantly different from those of the 20-μm-long metal pads, and both lengths show no discernible modulation. For longer metal pads, we find, as expected, that as the metal pad lengthens, the critical frequency decreases such that the same frequency may experience a greater degree of modulation. The modulated impedance magnitude dips below the baseline value but asymptotically approaches the baseline as the frequency and/or metal pad length increases.

To estimate the maximum DCVBP slope that appears in this data set, we can fit a line through the origin to each set of points. The steepest negative slope we observe is −223.8 mΩ/Ω, 95% confidence interval (CI(−0.2278, −0.2199)), for the 160-μm-long metal pad at 204.5 kHz.

C. LCC model fitting

We show that the data not only follow the qualitative trend predicted by the LCC models, but also quantitatively match the LCC slice model by performing a model fit for both the narrower device and the wider device. We use the LCC slice model for faster model convergence while retaining adequate accuracy. For each metal pad array device, we create an LCC model using the channel geometry and resistivity, then solve for the specific CPE parameter and CPE exponent for each pad that best fit the data. Specifically, we fix the LCC model's channel width and height to be the same as the measured values and set all other channel geometry (e.g., the lengths of the model's gaps and metal pads) to the designed values. The model's PBS resistivity is set to $\rho = 0.625\ \Omega$m. We then solve for the best fitting

CPE parameters, namely, q_{edl} (i.e., CPE parameter per unit area) and α, for each metal pad using nonlinear least squares optimization. We sought to minimize the MAE between the pad response values of the data and quadratic fits of the LCC model predictions. In Fig. 5, LCC model predictions for several cell diameters are shown as circles, while the quadratic fits through those circles are displayed as solid lines. We opted to minimize the MAE between the data and the quadratic curves, which are constrained to pass through the origin, because computing the LCC model's predicted pad response value for every gap response value represented in the data was too computationally expensive. We chose to minimize the MAE rather than the root-meansquare error (RMSE) to reduce the influence of any outliers in the data, but we found that minimizing the RMSE yielded nearly identical results. Below the plots in Fig. 5, we report the RMSE and MAE of the fitted LCC models in both absolute and relative terms. For example, in Fig. 5(b), the RMSE between the predicted pad response values of the LCC model and the measured pad response data, evaluated at each measured gap response value, is 3.75% of the root-mean-square value of the measured pad response data. Similarly, the MAE of the LCC model's predicted pad response values relative to the mean absolute value of the measured pad response data is 3.80%. For the narrower pad array device, Fig. 5(a) shows a similarly good model fit, with a relative RMSE of 4.23% and a relative MAE of 3.74%.

We found that in order to get an acceptable fit, it was necessary to allow the model to use CPEs rather than ideal capacitors, and to use different CPE parameters for each metal pad EDL. The underlying reason that each metal pad EDL would have different properties is unknown. Numerous values for the CPE parameters of an EDL between PBS and shiny platinum are reported in the literature (e.g., [42] found a specific CPE parameter of $q_{edl} = 0.1393\ \mathrm{Ss}^{\alpha}/\mathrm{m}^2$ with CPE exponent = 0.8012), but electrode/electrolyte interfaces are complex systems that can be unstable and difficult to model. Anything from metal film thickness and microstructure to chemical reactions at the interface could potentially alter the CPE parameters of an EDL. Furthermore, unlike the EDLs in the parallel platelike devices in [42], the EDLs in our devices operate within nonuniform electric fields, which may potentially cause their behavior to deviate from the CPE model due to nonlinear effects. Regardless, we do not seek to predict or explain the precise CPE parameter values of metal pad EDLs, only to explain the impedance modulation effects caused by metal pads while using CPEs as part of the LCC model.

IV. DISCUSSION

In this study, we have described a surprising phenomenon that can occur during the operation of a microfluidic technology called metal pad sensing (MPS). We have developed a theory for the CVBP (and DCVBP) in MPS using both FEA and LCC modeling. By leveraging these models, CVBP and DCVBP effects can be predicted not only in MPS, but potentially in a multitude of natural and engineered systems. The paradox can either be avoided or exploited to design scientific experiments or improve device designs.

The purpose of MPS is to modulate an RPS impedance signal using metal pads. By modulating the signal, we gain information about the cell's position along the microchannel without requiring additional electrodes or high-speed cameras. This is applicable to any

technology that uses a cell's transit time as a biomarker or distinguishing feature, as in [5,9–11,13]. Compared to other RPS signal modulation techniques, MPS-based modulation has a number of advantages. Metal pads can be added to an RPS device with minimal changes in the fabrication process, whereas the method of [43] requires a complex electrode design. Another benefit of RPS signal modulation is coincidence resolution [43,44], where signal processing can resolve overlapping RPS signals caused by multiple particles simultaneously occupying the sensing region. Many microfluidic devices squeeze cells using fixed-width channels to interrogate mechanical properties [10,11,13,45]. These channels cannot be modulated by varying the channel width as in [5], but metal pads can be readily applied to enable coincidence resolution, leading to higher throughput and less data loss.

Regardless of the reason for RPS signal modulation, stronger modulation may be desired to increase the signal-to-noise ratio (SNR). In the context of coincidence resolution, stronger modulation also increases the signal-to-interference ratio (SIR) when using correlation-based detection or matched filtering [46]. For MPS, in particular, the negative troughs caused by the CVBP make an otherwise unipolar signal bipolar, greatly improving the SIR. Both SNR and SIR are crucial factors that influence the performance of automatic signal detection and estimation algorithms in various RPS technologies geared towards rapid disease diagnosis. Therefore, understanding and maximizing the CVBP effect could play a role in improving applications of future RPS devices such as disease detection or monitoring.

The CVBP may also play a role in other applications. It is likely to arise in analogous systems in other branches of science which have an electrical circuit analogy with an analogous complex impedance, e.g., mechanical, acoustic, thermal, hydraulic, viscoelastic, or microelectromechanical systems (MEMS). For example, in the mechanical-electrical "impedance analogy" [47], force is analogous to voltage, velocity is analogous to current, and, when describing an oscillating mechanical component at steady state, the ratio of force to velocity is the complex mechanical impedance. Damping and compliance are analogous to resistance and capacitance, respectively. Mass is analogous to inductance, which we did not consider in this work. Perhaps there exists a system modeled by a two-port mechanical circuit with only damping and compliance components (or only damping and mass), in which increasing the mechanical impedance of one or more paths causes the total mechanical impedance to decrease. Researchers analyzing or designing systems in these or other domains could benefit greatly by gaining a better understanding of the CVBP and DCVBP.

ACKNOWLEDGMENTS

We thank R. Falcón-Banchs, A. Lai, and C. Pierce for providing the MCF-7 cells used in these experiments. This work was supported by National Institutes of Health (Grants No. R01EB024989 and No. 2R01EB024989-05), the Agilent University Relations: ABP program (No. 4757), and the Robert N. Noyce Memorial Fellowship in Microelectronics.

APPENDIX: LCC VOXEL MODEL

The LCC voxel model treats the MPS device channel as a 2D rectangular mesh of resistors, with capacitors (or CPEs) connecting to the metal pads below. The fineness of the mesh is determined by the voxel size. As an illustrative example, Fig. 6(a) shows an 80μm × 20μm × 20μm ($L \times W \times H$) MPS channel with a 40-μm-long metal pad at the center, divided into equal-volume "channel voxels" of size $10\ \mu m \times 20\ \mu m \times 10\ \mu m$ ($L \times W \times H$), which results in a total of 16 channel voxels arranged in an 8 × 2 grid. Each channel voxel edge that is oriented into the page is assumed to be an isopotential, represented by a circuit node called a "voxel node." In this example, there are 27 voxel nodes, arranged in a 9 × 3 grid. Each metal pad is also assumed to be an isopotential, represented by a circuit node called a "pad node." Adjacent voxel nodes are connected via resistors both horizontally and vertically. We will now separately consider the horizontal and vertical resistors.

The horizontal resistors correspond to another grid of voxels, offset from the original grid. In this example, there are 24 horizontal resistor voxels, arranged in an 8 × 3 grid, but they do not all have equal volume. The horizontal resistor voxels in the top and bottom rows have half the height (and thus, half the volume) of those in the interior (i.e., the middle row). The resistance of each horizontal resistor is defined by the geometry of its corresponding voxel as $\rho l/(Wh)$, where ρ is the PBS resistivity, l is the voxel length (along the horizontal axis), W is the channel width, and h is the voxel height (along the vertical axis). In this example, the horizontal resistors in the middle row each have a resistanceof $r = \rho \times 10\ \mu m/(20\ \mu m \times 10\ \mu m) = 31.25\ k\Omega$ using $\rho = 0.625\ \Omega m$. In comparison, the horizontal resistors in the top and bottom rows have half the height, resulting in twice the resistance, $2r = 62.5\ k\Omega$.

The treatment of vertical resistors is analogous. The vertical resistors correspond to yet another grid of voxels, offset from the original grid. In this example, there are 18 "vertical resistor voxels," arranged in a 9 × 2 grid. The vertical resistor voxels in the leftmost and rightmost columns have half the length (along the horizontal axis) of those in the interior. The resistance of each vertical resistor is defined by the geometry of its corresponding voxel as $\rho h/(Wl)$, where h is the voxel height along the vertical axis. In this example, since we are using voxels whose length and height are equal, the vertical resistors (except for those in the leftmost and rightmost columns) have the same resistance r as the horizontal resistors. The vertical resistors in the leftmost and rightmost columns have resistance $2r$.

We now add the capacitors (or CPEs) that represent the metal pad EDLs. For each voxel node on the bottom row, we call the channel voxel immediately to the left the "left voxel" and the channel voxel immediately to the right the "right voxel." If both left and right voxels of a given voxel node are in contact with a metal pad, then the voxel node is connected to the pad node via a capacitor with capacitance $C_s W(l_{left} + l_{right})/2$, where C_s is the EDL's specific capacitance (i.e., capacitance per unit area), W is the channel width, and l_{left} and l_{right} are the lengths of the left and right voxels, respectively. If the left voxel does not contact a metal pad or does not exist (i.e., the voxel node is on the left edge of the metal pad or left edge of the channel), then l_{left} is set to zero. The same is true for the right voxel and

$l_{right.}$. In the example shown in Fig. 6(a), all but the leftmost and rightmost capacitors have capacitance $c = C_s \times 20\ \mu m \times (10\ \mu m + 10\ \mu m)/2 = 40$ pF assuming $C_s = 0.2$ F/m^2. The leftmost and rightmost capacitors connect to the left and right edges of the metal pad, and have half the capacitance $c/2 = 20$ pF.

Using the rules as described, the LCC voxel model is capable of simulating an empty MPS channel, but we also wish to model the introduction of a cell. Just like the R + R/C model and the LCC slice model (Sec. II A), the LCC voxel model relies on the FEA model to simulate the total ΔR caused by the presence of a cell within the channel. Unlike with the LCC slice model, however, we cannot simply add a fraction of ΔR to each resistor according to the fraction of the cell's volume contained within each resistor's "block." Instead, we assume that the relative resistance increase of each resistor (whether horizontal or vertical) is proportional to the cell's volume contained within the corresponding resistor voxel, relative to the resistor voxel's volume.

For example, Fig. 6(b) shows a cell intersecting four horizontal resistor voxels (outlined in gray), which are numbered 3, 19, 20, and 37. We previously determined that the resistor corresponding to voxel 19 has a baseline value of $R_{19} = r = 31.25$ kΩ. Now, we find voxel 19 to have volume $v_{19} = v = lWh = 10\ \mu m \times 20\ \mu m \times 10\ \mu m = 2$ fL. Next, we define Δv_{19} as the partial volume of the cell contained within voxel 19 and estimate it in practice by subdividing the voxel into subvoxels and running an algorithm based on marching cubes [48]. Finally, we define the relative resistance increase $\Delta R_{19}/R_{19} = \beta \Delta v_{19}/v_{19}$, where β is a scalar factor soon to be determined. For voxel 20, the relative resistance increase $\Delta R_{20}/R_{20}$ is defined in the same manner. Since voxels 3 and 37 are only half the size of voxels 19 and 20, they each have half the volume, $v/2 = 1$ fL, but the procedure for determining the relative resistance increase is the same. Figure 6(c) shows the same procedure, but for the vertical resistors. In this example, the cell intersects four vertical resistor voxels (numbered 11, 12, 28, and 29), each having volume v. The relative resistance increase of each resistor is again $\Delta v/v$ times an unknown scalar β.

We define a function $\mathscr{R}(\beta)$ that computes the total resistance of the circuit as a function of β. For $\beta = 0$, it returns the baseline resistance, which we denote as R_0. If we choose $\beta = 1$, we are assuming that each resistor R_i experiences a relative resistance increase $\Delta R_i/R_i = \Delta v_i/v_i$. In practice, we compute $\mathscr{R}(\beta = 1)$ and find that it always falls short of $R_0 + \Delta R$, the channel resistance predicted by the FEA model. We use Muller's root-finding method [49] to find the appropriate value β^* such that $\mathscr{R}(\beta^*) - (R_0 + \Delta R) = 0$. In this example, a cell of diameter $d = 12.5\ \mu m$ causes a total resistance increase of $\Delta R = 6.951$ kΩ over the baseline resistance of $R_0 = 125$ kΩ. After four iterations, Muller's method returns a value of $\beta^* = 2.3766$.

The primary reason the LCC voxel model is more accurate than the LCC slice model is that it allows for curved isopotential surfaces, whereas the linear circuit layout of the LCC slice model implicitly assumes purely vertical isopotential surfaces. The contour plots in Fig. 6(d) show a 2D side view of the isopotential surfaces of the previously described MPS channel computed by an LCC voxel model using voxels of size $1\ \mu m \times 20\ \mu m \times 1\ \mu m$ ($L \times W \times H$). The top plot shows how the metal pad gives rise to curved isopotential surfaces. The

bottom plot shows how the introduction of a cell further distorts the isopotential surfaces. These contour plots can be compared with those in Fig. 6(e), which show isopotential surfaces computed by the FEA model along with electric field lines, which are everywhere perpendicular to the isopotential surfaces. Bode and Nyquist plots of predicted impedance spectra shown in Fig. 6(f) confirm that the LCC voxel model and FEA model match very closely.

References

[1]. Coulter WH, Means for counting particles suspended in a fluid, U.S. Patent No. 2,656,508 (20 October 1953).

[2]. DeBlois RW and Bean CP, Counting and sizing of submicron particles by the resistive pulse technique, Rev. Sci. Instrum. 41, 909 (1970).

[3]. Gregg EC and Steidley KD, Electrical counting and sizing of mammalian cells in suspension, Biophys. J. 5, 393 (1965). [PubMed: 5861698]

[4]. Kubitschek HE, Electronic counting and sizing of bacteria, Nature (London) 182, 234 (1958). [PubMed: 13577794]

[5]. Balakrishnan KR, Whang JC, Hwang R, Hack JH, Godley LA, and Sohn LL, Node-pore sensing enables label-free surface-marker profiling of single cells, Anal. Chem. 87, 2988 (2015). [PubMed: 25625182]

[6]. Chapman MR and Sohn LL, Label-free resistive-pulse cytometry, in Methods in Cell Biology (Elsevier, Amsterdam, 2011), Vol. 102, pp. 127–157. [PubMed: 21704838]

[7]. Gawad S, Schild L, and Renaud PH, Micromachined impedance spectroscopy flow cytometer for cell analysis and particle sizing, Lab Chip 1, 76 (2001). [PubMed: 15100895]

[8]. Satake D, Ebi H, Oku N, Matsuda K, Takao H, Ashiki M, and Ishida M, A sensor for blood cell counter using MEMS technology, Sens. Actuators B 83, 77 (2002).

[9]. Saleh OA and Sohn LL, Direct detection of antibody-antigen binding using an on-chip artificial pore, Proc. Natl. Acad. Sci. USA 100, 820 (2003). [PubMed: 12552089]

[10]. Chen J, Zheng Y, Tan Q, Shojaei-Baghini E, Zhang YL, Li J, Prasad P, You L, Wu XY, and Sun Y, Classification of cell types using a microfluidic device for mechanical and electrical measurement on single cells, Lab Chip 11, 3174 (2011). [PubMed: 21826361]

[11]. Kim J, Han S, Lei A, Miyano M, Bloom J, Srivastava V, Stampfer MR, Gartner ZJ, LaBarge MA, and Sohn LL, Characterizing cellular mechanical phenotypes with mechano-node-pore sensing, Microsyst. Nanoeng. 4, 17091 (2018). [PubMed: 29780657]

[12]. Kim J, Li B, Scheideler OJ, Kim Y, and Sohn LL, Visco-node-pore sensing: A microfluidic rheology platform to characterize viscoelastic properties of epithelial cells, iScience 13, 214 (2019). [PubMed: 30870780]

[13]. Zhou Y, Yang D, Zhou Y, Khoo BL, Han J, and Ai Y, Characterizing deformability and electrical impedance of cancer cells in a microfluidic device, Anal. Chem. 90, 912 (2018). [PubMed: 29172457]

[14]. Hoffman RA and Britt WB, Flow-system measurement of cell impedance properties, J. Histochem. Cytochem. 27, 234 (1979). [PubMed: 374580]

[15]. Hoffman RA, Johnson TS, and Britt WB, Flow cytometric electronic direct current volume and radiofrequency impedance measurements of single cells and particles, Cytom.: J. Int. Soc. Anal. Cytol. 1, 377 (1981).

[16]. Zheng Y, Shojaei-Baghini E, Wang C, and Sun Y, Microfluidic characterization of specific membrane capacitance and cytoplasm conductivity of singlecells, Biosens. Bioelectron. 42, 496 (2013). [PubMed: 23246657]

[17]. Foster KR and Schwan HP, Dielectric properties of tissues, in CRC Handbook of Biological Effects of Electromagnetic Fields (CRC Press, Boca Raton, FL, 1986), pp. 27–96.

[18]. De Ninno A, Errico V, Bertani FR, Businaro L, Bisegna P, and Caselli F, Coplanar electrode microfluidic chip enabling accurate sheathless impedance cytometry, Lab Chip 17, 1158 (2017). [PubMed: 28225104]

[19]. Dong A, Sohn L, and Lustig M, Data and Software for "Metal pad-enhanced resistive pulse sensor reveals complex-valued Braess paradox" (2023), doi:10.5281/zenodo.7771195.

[20]. https://github.com/sohnlab/CVBP_in_MPS.

[21]. Braess D, Nagurney A, and Wakolbinger T, On a paradox of traffic planning, Transport. Sci. 39, 446 (2005).

[22]. Altman E, Kambley V, and Kamedaz H, A Braess type paradox in power control over interference channels, in 2008 Sixth International Symposium on Modeling and Optimization in Mobile, Ad Hoc, and Wireless Networks and Workshops (IEEE, New York, 2008), pp. 555–559.

[23]. Xia Y and Hill DJ, Dynamic Braess's paradox in complex communication networks, IEEE Trans. Circuits Syst. II Express Briefs 60, 172 (2013).

[24]. Kameda H, Altman E, Kozawa T, and Hosokawa Y, Braess-like paradoxes in distributed computer systems, IEEE Trans. Automat. Contr. 45, 1687 (2000).

[25]. Baillieul J, Zhang B, and Wang S, The Kirchhoff-Braess paradox and its implications for smart microgrids, in 2015 54th IEEE Conference on Decision and Control (CDC) (IEEE, New York, 2015), pp. 6556–6563.

[26]. Coletta T and Jacquod P, Linear stability and the Braess paradox in coupled-oscillator networks and electric power grids, Phys. Rev. E 93, 032222 (2016). [PubMed: 27078359]

[27]. Pala MG, Baltazar S, Liu P, Sellier H, Hackens B, Martins F, Bayot V, Wallart X, Desplanque L, and Huant S, Transport Inefficiency in Branched-Out Mesoscopic Networks: An Analog of the Braess Paradox, Phys. Rev. Lett. 108, 076802 (2012). [PubMed: 22401236]

[28]. Sousa AA, Chaves A, de Aquino Farias G, and Peeters FM, Braess paradox at the mesoscopic scale, Phys. Rev. B 88, 245417 (2013).

[29]. Banerjee A and Bej P, Braess paradox in a quantum network, Phys. Rev. A 104, 052622 (2021).

[30]. Barbosa ALR, Bazeia D, and Ramos JGGS, Universal Braess paradox in open quantum dots, Phys. Rev. E 90, 042915 (2014).

[31]. Case DJ, Liu Y, Kiss I, Angilella J-R, and Motter AE, Braess's paradox and programmable behaviour in microfluidic networks, Nature (London) 574, 647 (2019). [PubMed: 31645762]

[32]. Donovan GM, Biological version of Braess' paradox arising from perturbed homeostasis, Phys. Rev. E 98, 062406 (2018).

[33]. Kippenberger S, Meissner M, Kaufmann R, Hrgovic I, Zöller N, and Kleemann J, Tumor neoangiogenesis and flow congestion: A parallel to the Braess paradox? Circ. Res. 119, 711 (2016). [PubMed: 27587409]

[34]. Cohen JE and Horowitz P, Paradoxical behaviour of mechanical and electrical networks, Nature (London) 352, 699 (1991).

[35]. Nagurney LS and Nagurney A, Physical proof of the occurrence of the Braess paradox in electrical circuits, Europhys. Lett. 115, 28004 (2016).

[36]. Grahame DC, The electrical double layer and the theory of electrocapillarity, Chem. Rev. 41, 441 (1947). [PubMed: 18895519]

[37]. DeBlois RW, Bean CP, and Wesley RKA, Electrokinetic measurements with submicron particles and pores by the resistive pulse technique, J. Colloid Interface Sci. 61, 323 (1977).

[38]. Maxwell JC, A Treatise on Electricity and Magnetism, 3rd ed. (Clarendon Press, Oxford, 1904), Vol. 1, p. xi.

[39]. Schwan HP, Electrical properties of cells: Principles, some recent results, and some unresolved problems, in The Biophysical Approach to Excitable Systems (Springer, Berlin, 1981), pp. 3–24.

[40]. Svilainis L and Dumbrava V, Test fixture compensation techniques in impedance analysis, Elektronika ir Elektrotechnika 87, 37 (2008).

[41]. Lewis JP, Fast normalized cross-correlation, industrial light and magic (unpublished).

[42]. Koklu A, Sabuncu AC, and Beskok A, Rough gold electrodes for decreasing impedance at the electrolyte/electrode interface, Electrochim. Acta 205, 215 (2016). [PubMed: 27695132]

[43]. Liu R, Wang N, Kamili F, and Sarioglu AF, Microfluidic codes: A scalable multiplexed electronic sensor for orthogonal detection of particles in microfluidic channels, Lab Chip 16, 1350 (2016). [PubMed: 27021807]

[44]. Kellman MR, Rivest FR, Pechacek A, Sohn LL, and Lustig M, Node-pore coded coincidence correction: Coulter counters, code design, and sparse deconvolution, IEEE Sens. J. 18, 3068 (2018). [PubMed: 29988953]

[45]. Shelby JP, White J, Ganesan K, Rathod PK, and Chiu DT, A microfluidic model for single-cell capillary obstruction by Plasmodium falciparum-infected erythrocytes, Proc. Natl. Acad. Sci. USA 100, 14618 (2003). [PubMed: 14638939]

[46]. Turin G, An introduction to matched filters, IEEE Trans. Inform. Theory 6, 311 (1960).

[47]. Busch-Vishniac IJ, Electromechanical Sensors and Actuators (Springer-Verlag, New York, 1998).

[48]. Lorensen WE and Cline HE, Marching cubes: A high resolution 3D surface construction algorithm, SIGGRAPH Comput. Graph. 21, 163 (1987).

[49]. Muller DE, A method for solving algebraic equations using an automatic computer, Math. Tables Other Aids Comput. 10, 208 (1956).

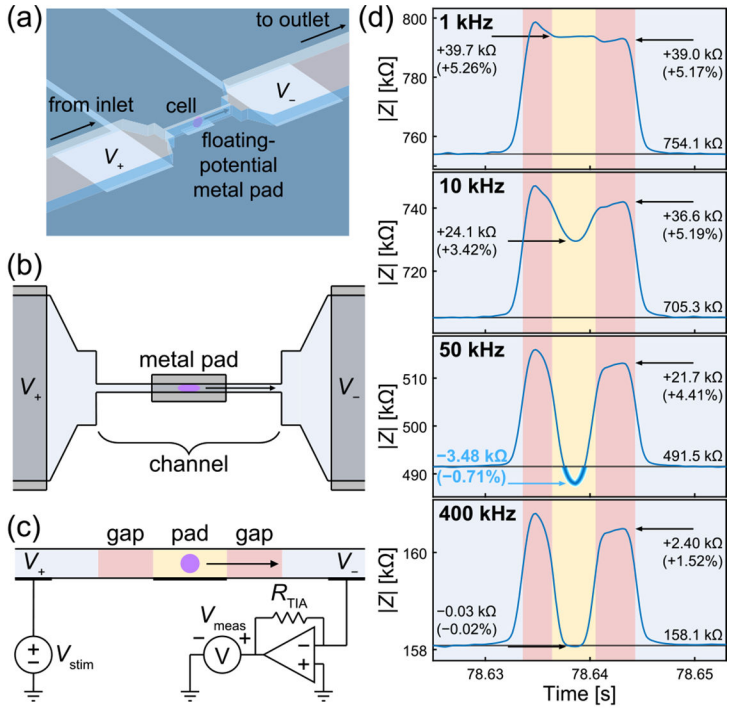

FIG. 1.

Metal pad sensing device and surprising results of cell transit experiment. (a) Three-dimensional render of MPS device (channel enlarged to show detail). (b) Top view schematic with the flow direction as indicated. (c) Side view schematic shows the channel divided into gaps and pad segments and the impedance measurement circuit. (d) Experimental data show the impedance measured at four different frequencies as a cell transits though a device. The channel dimensions were 200 μm × 10 μm × 18 μm ($L \times W \times H$), with an 80-μm-long metal pad and 1000 μm × 1000 μm electrodes. At all frequencies, the cell causes an impedance increase while traversing through a gap. At higher frequencies, an unexpected result occurs: The cell causes an impedance decrease while traversing over the pad. This is the complex-valued Braess paradox.

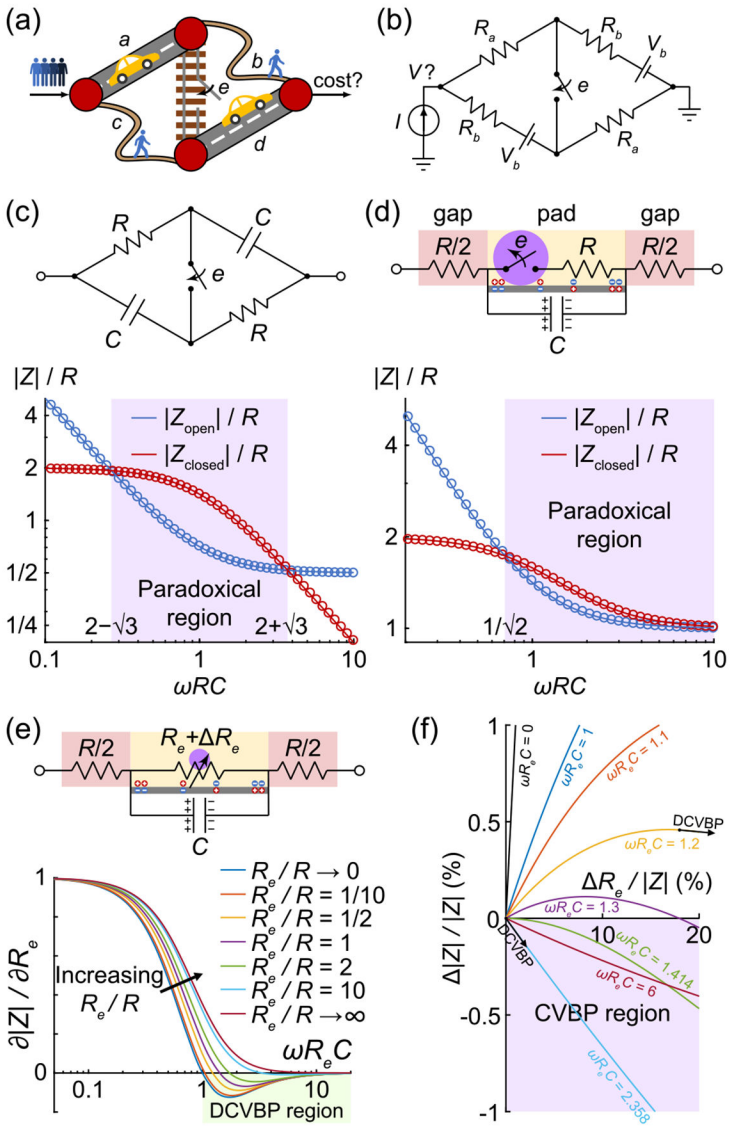

FIG. 2.

From traffic network to MPS circuit model: Connections between different Braess networks. (a) Classical Braess paradox: Adding path *e* counterintuitively increases the total cost (travel time). (b) Electrical Braess paradox: Analogous DC circuit exhibits identical behavior. (c) Complex-valued Braess paradox: Adding path *e* counterintuitively increases impedance magnitude near the RC cutoff frequency. Normalized impedance magnitude is plotted against normalized frequency, both axes logarithmically scaled. Lines are analytical; circles are experimental data ($R_a = 10.01$ kΩ, $R_d = 9.999$ kΩ, $C_b = 9.98$ nF, $C_c = 9.92$ nF, $R = (R_a + R_d)/2$, and $C = (C_b + C_c)/2$). The subscript of each component corresponds to the letter of each path as depicted in (a). (d) $R + C/(R)$ circuit: Simplistic approximation of the MPS device also exhibits the CVBP. Normalized impedance magnitude is plotted against normalized frequency, both axes logarithmically scaled. Lines are analytical; circles

are experimental data (same circuit components as (c) except without capacitor C_c). (e) Differential CVBP (DCVBP): This version of the CVBP applies to differential changes in R_e. The derivative of impedance magnitude with respect to R_e, plotted against normalized frequency (logarithmically scaled), reveals different paradoxical regions for different ratios of R_e/R as well as different maximum paradoxical effects. (f) For the same circuit as in (e), with $R_e = R$, normalized change in channel impedance magnitude is plotted against normalized change in pad segment resistance. Each curve depicts a different normalized frequency. Any point in the bottom right quadrant indicates CVBP, while any point at which the tangent line has negative slope indicates DCVBP.

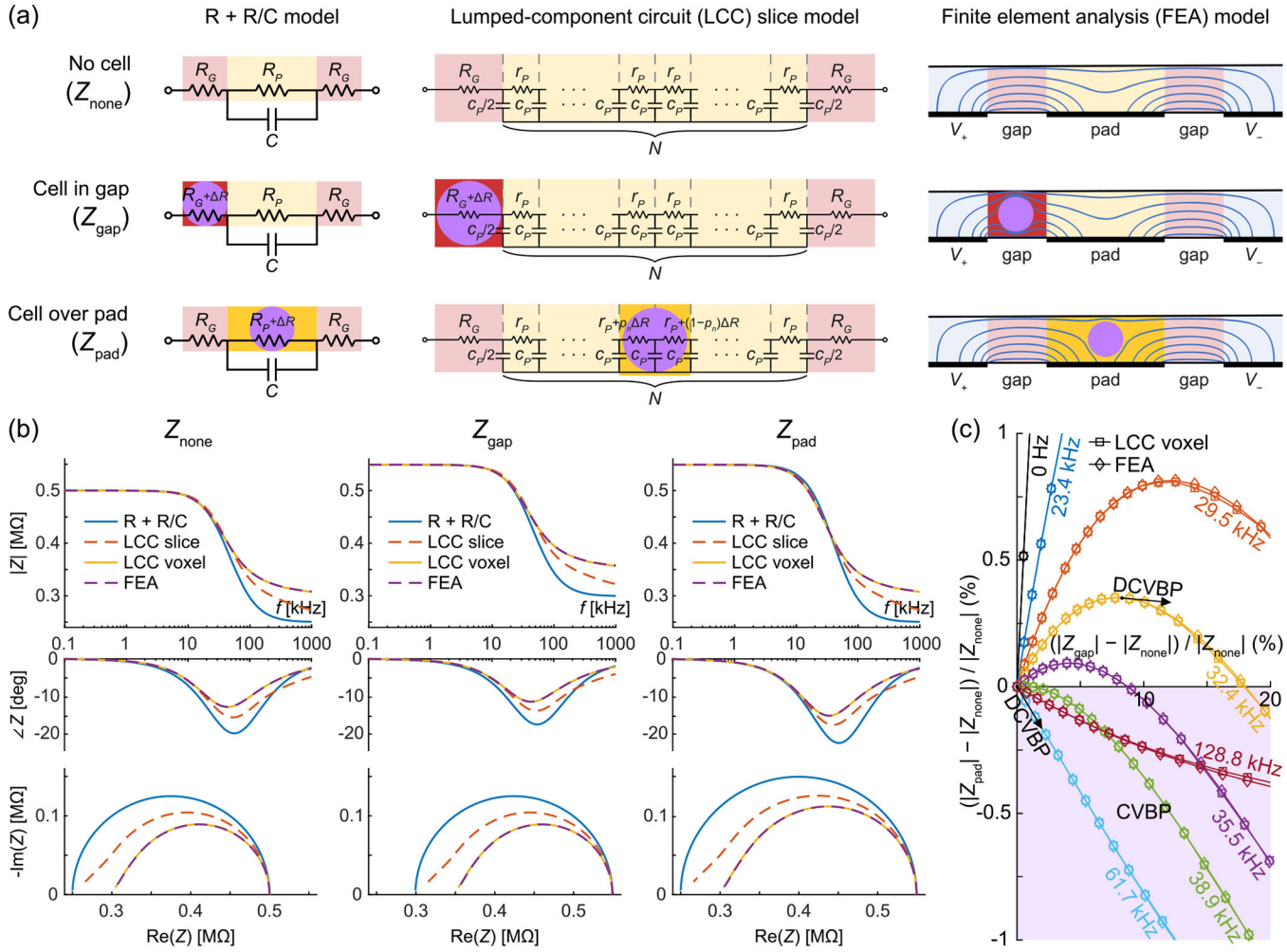

FIG. 3.

Comparison of three MPS device models. (a) Table of diagrams depicts three models (columns) of a single-pad MPS device under three different conditions (rows). The lumped-component circuit (LCC) model can be viewed as a higher-fidelity version of the R + R/C model, meant to more closely match the 3D finite element analysis (FEA) model. It achieves this by breaking the distributed EDL impedance into many small compartments, resulting in an RC network. In addition to the channel, the FEA model diagram includes the electrodes V_+ and V_- as well as current streamlines between them. The additional impedance of the electrolyte solution and electrode EDLs outside of the channel can also be included in both circuit-based models using additional resistors and RC networks, but it is negligible at our frequencies of interest. For the purposes of this figure, this additional impedance is not considered in any of the models. (b) Impedance spectra under three different conditions for all three models, depicted as Bode and Nyquist plots, highlight the differences between the R + R/C model and the LCC model. (c) The “pad vs gap response diagram” for the LCC and FEA models confirms that they predict almost identical behavior up to a gap response of 10% above baseline. This plot can be contrasted with Fig. 2(f), which closely resembles the pad vs gap response diagram of the R + R/C model.

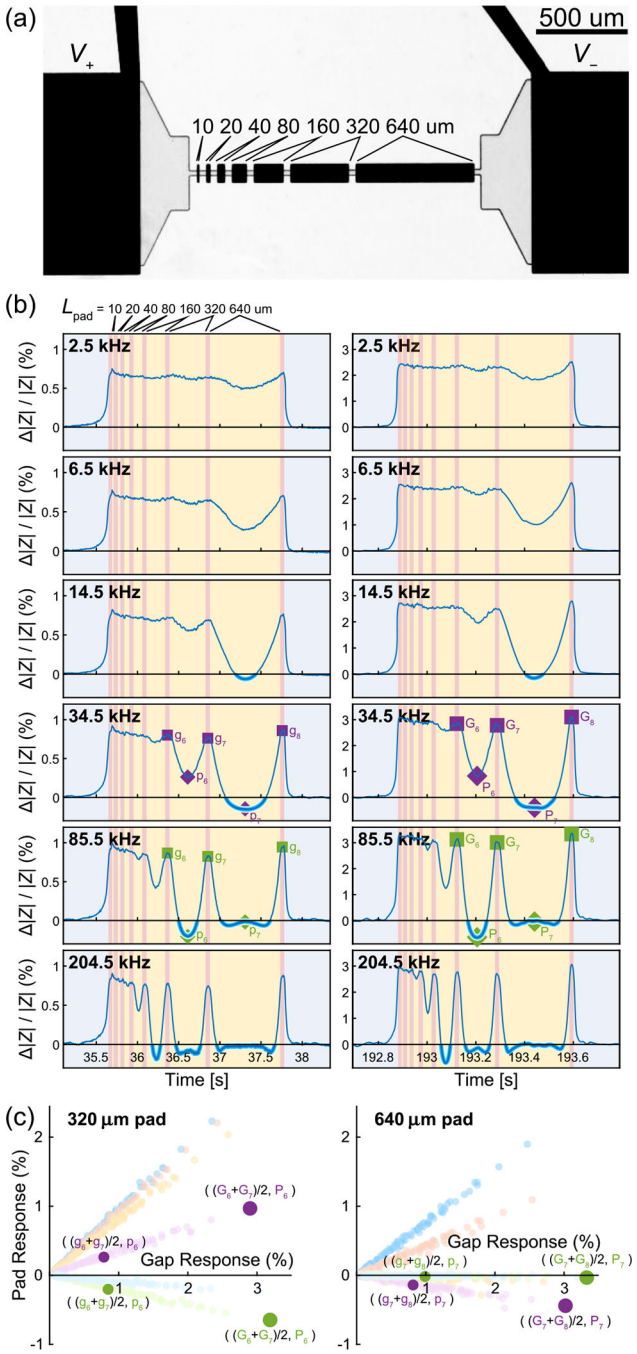

FIG. 4.

Study of impedance modulation using metal pad array devices. (a) Microscope image of a metal pad array device shows seven pads of varying lengths patterned within a long channel ($L_{\text{total}} = 1590$ µm, $W = 24.2$ µm, and $H = 28.5$ µm), separated by gaps of length $L_G = 40$ µm. (b) As a cell traverses the channel from left to right, it passes through each gap and pad segment, modulating the measured impedance by a different amount. Normalized impedance magnitude is plotted against time for six frequencies, each portion of the signal highlighted according to whether the cell occupies a gap [red (darker)] or pad segment [yellow (lighter)].

Left, smaller cell example; right, larger cell. Special points are marked (as squares and diamonds) to help illustrate the construction of the pad vs gap response diagram. (c) Left, construction of 320-μm-long pad vs. gap response diagram using specially marked points from (b); right, same, but for 640 - μm-long pad.

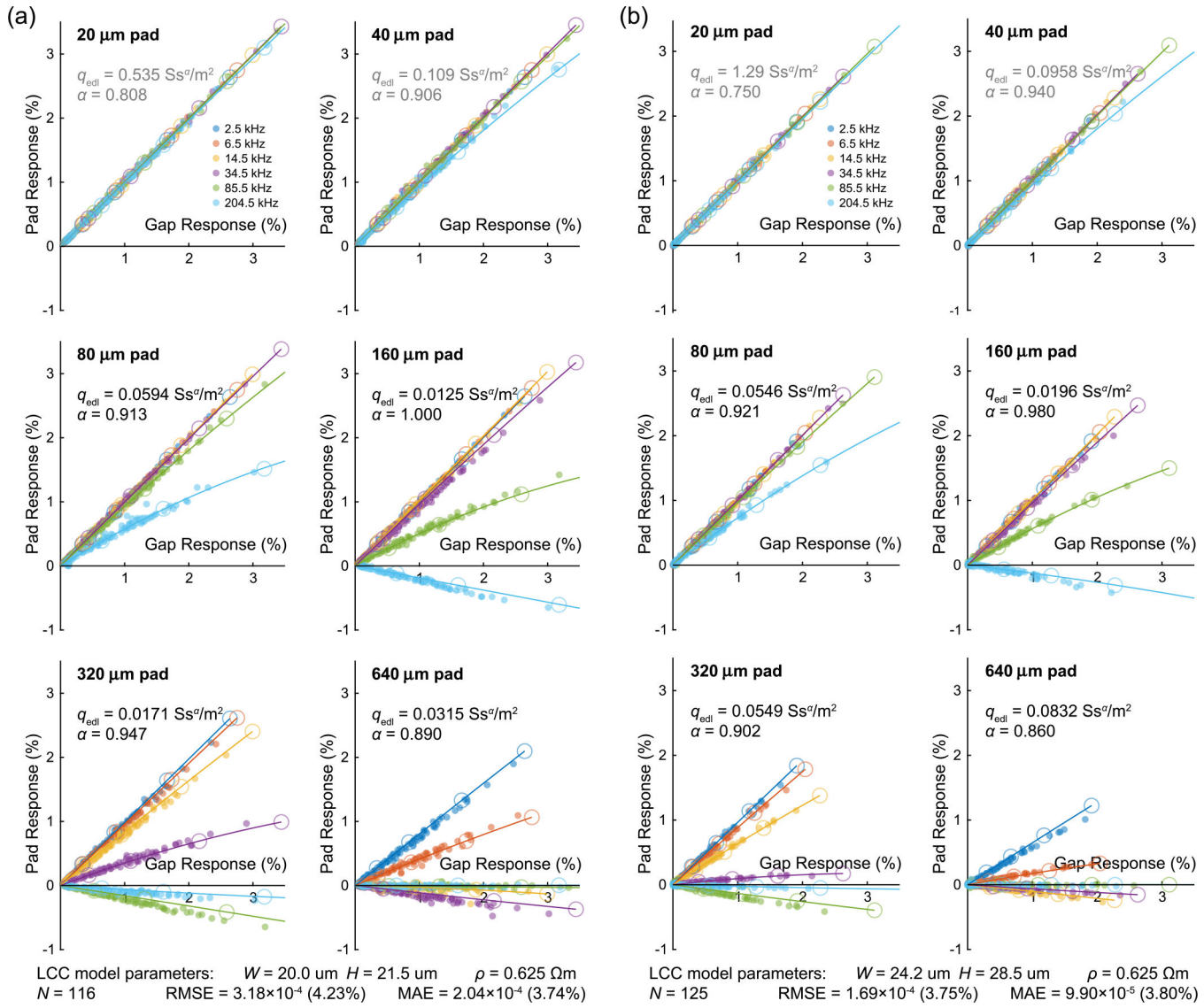

FIG. 5.

Pad vs gap response diagrams simultaneously reveal the effects of pad length, frequency, and cell size. (a) Pad vs gap response diagrams for narrower (W = 20.0 μm, H = 21.5 μm) metal pad array. Each subplot corresponds to a different length pad. N = 116 cell transit events are plotted as points on each axis, with each color depicting a different frequency. Circles are the LCC model's predicted pad vs gap responses for a few different cell diameters. Solid lines are quadratic fits to the LCC model predictions. Fitted CPE parameters q_{edl} and α are shown for each pad length. Root-mean-square error (RMSE) and MAE of the model fit are reported below. (b) Same as (a), but for the wider (W = 24.2 µm, H = 28.5 µm) pad array, N = 125 cell transit events.

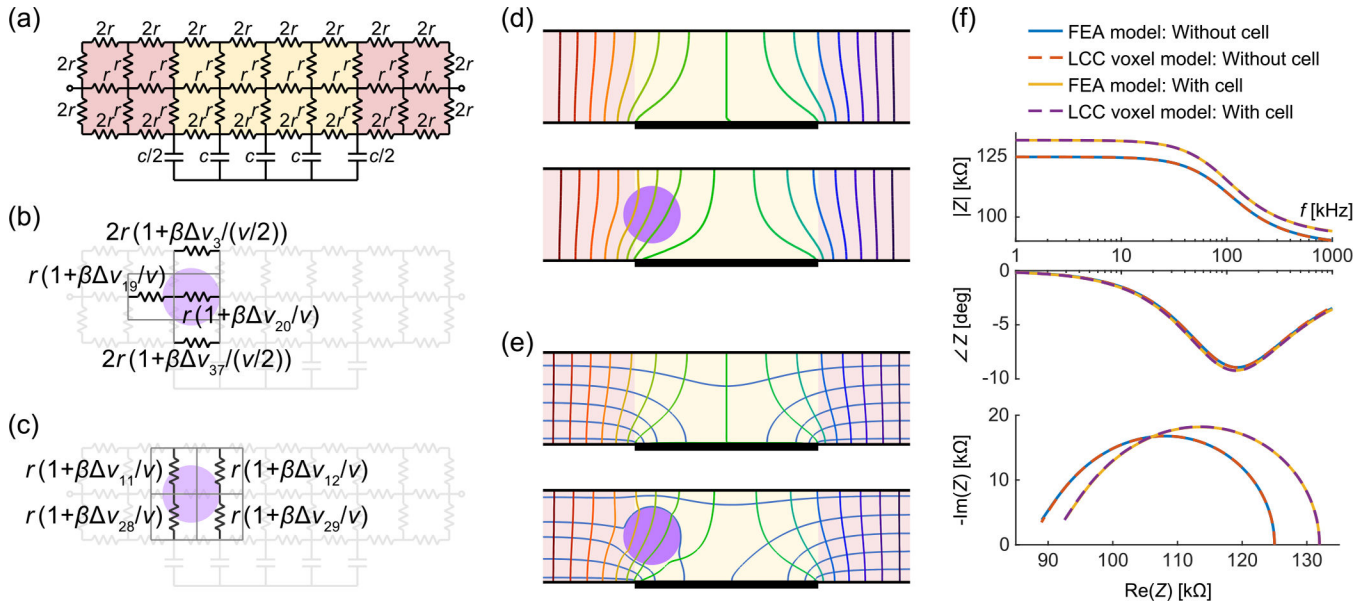

FIG. 6.

(a) LCC voxel model of a single-pad MPS device channel at baseline (no cell), 80 μm × 20 μm × 20 μm($L \times W \times H$), with a 40-μm-long metal pad at the center. Gaps are highlighted in red (dark gray); the pad segment is highlighted in yellow (light gray). The channel is divided into 16 "channel voxels," each of size 10 μm × 20 μm × 10 μm ($L \times W \times H$). Impedance is computed between the left and right terminals. (b) Each horizontal resistor is associated with a "horizontal resistor voxel." These voxels do not all have the same volume. When a cell intersects a horizontal resistor voxel (here, the cell intersects four voxels, which are outlined in gray), the corresponding horizontal resistor increases its relative resistance in proportion to the partial volume of the cell contained within that voxel, relative to the volume of the voxel itself. Each resistor's relative resistance increase is also proportional to an unknown scalar β, which is determined through optimization. (c) Each vertical resistor is associated with a "vertical resistor voxel." These voxels do not all have the same volume. When a cell intersects a vertical resistor voxel (here, the cell intersects four voxels, which are outlined in gray), the corresponding vertical resistor increases according to the same rule that governs horizontal resistors. (d) Contour plots, computed by the LCC voxel model using voxels of size 1 μm × 2 0 μm × 1 μm ($L \times W \times H$), show a 2D side view of isopotential surfaces, both with and without a cell present. (e) Contour plots, computed by the FEA model, show a 2D side view of isopotential surfaces, both with and without a cell present. Additionally, electric field lines are shown. (f) Bode and Nyquist plots confirm that the LCC voxel model and FEA model predict very similar impedance spectra both with and without a cell present.